Journal Pre-proof

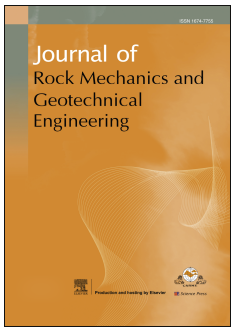

Numerical investigation of wellbore damage due to drill string lateral vibration

Hadi Haghgouei, Anders Nermoen, Alexandre Lavrov

PII: S1674-7755(24)00370-6

DOI: https://doi.org/10.1016/j.jrmge.2024.04.032

Reference: JRMGE 1689

To appear in: *Journal of Rock Mechanics and Geotechnical Engineering*

Received Date: 5 December 2023

Revised Date: 15 March 2024

Accepted Date: 27 April 2024

Please cite this article as: Haghgouei H, Nermoen A, Lavrov A, Numerical investigation of wellbore damage due to drill string lateral vibration, *Journal of Rock Mechanics and Geotechnical Engineering*, https://doi.org/10.1016/j.jrmge.2024.04.032.

Full Length Article

Numerical investigation of wellbore damage due to drill string lateral vibration

Hadi Haghgouei[a,*], Anders Nermoen[b], Alexandre Lavrov[a]

[a] *Faculty of Engineering, Department of Geoscience and Petroleum, Norwegian University of science and Technology (NTNU), Trondheim, Norway*

[b] *Energy & Technology division, NORCE Norwegian Research Center AS, Oslo, Norway*

Abstract: During drilling operations, cyclic loading is exerted on the wellbore wall by the vibrations of the drill string. This loading could lead to rock fatigue, which in turn might result in wellbore failure. In this study, a numerical model is developed to simulate the effects of repeated loading on rock fatigue and failure. The simulation is based on an elasto-plastic constitutive model coupled with a damage mechanics approach, which allows us to examine the wellbore instability due to drill string vibrations. The model is verified with the existing data in the literature related to experiments on impact of a steel ball against a curved wall. The findings indicate that cyclic loading increases the development of plastic strain around the wellbore significantly compared to static conditions, promoting rock fatigue. Furthermore, the cyclic loading expands the radius of the yielded zone substantially, a critical factor for maintaining wellbore integrity. The proposed model can be used to evaluate the wellbore stability under repetitive loading caused by the drill string action.

Keywords: Wellbore stability, damage mechanics, fatigue modeling, drill string vibration

1. Introduction

One of the main problems in petroleum industry is wellbore instability (Singh et al., 2019), and engineers frequently encounter wellbore instability as one of the primary challenges during drilling operations (Pašić et al., 2007). According to Ma et al. (2022), wellbore instability is principally attributed to two main categories of variables: objective and subjective variables. Objective variables are largely determined by the rock type, mechanical properties of the rock, in-situ stress conditions, and overall geological features. The objective variables are immutable but can be precisely identified and managed during the drilling process by experienced drillers. On the other hand, subjective variables are chiefly related to the disturbance caused by the drilling activities, such as the wellbore trajectory, variations in the wellbore pressure and temperature, the drilling fluid chemistry, and drill string impact load on the wellbore (Ma et al., 2022).

In an alternative classification provided by Pasic et al. (2007), the underlying causes of wellbore instability are divided into two main classes. The first involves physicochemical interactions between the rock—particularly shale formations—and the drilling fluid. The second category encompasses mechanical reasons, such as the effects of drill string collisions with the wellbore wall, variations in rock mechanical properties, and stress distribution around the wellbore (Pašić et al., 2007).

Within scholarly research, considerable attention has been paid to the various elements that fall under each classification scheme for wellbore instability, be it objective and subjective variables or alternative classifications such as those outlined by Pasic et al. (2007). However, there is a marked lack of research focusing on wellbore instability caused by drill string impact on the wellbore wall, especially in scenarios involving repetitive impacts of the drill string.

Wellbores typically experience forces that are dynamic in nature rather than static (Meng et al., 2021), and drilling operations often result in the wellbore being subjected to repeated cycles of loading (Meng et al., 2020). Recognizing the cyclic loading on the wellbore wall and understanding the mechanisms behind it is crucial for investigating the stability of a wellbore over both short and long period of time (Meng et al., 2021).

The focus here is to model degradation of material strength when exposed to repeated impacts at stress levels that would be insufficient to cause failure individually.

Santos et al. (1999) argue that the primary cause of wellbore enlargement is not the physicochemical interaction between the drilling fluid and rock but is due to drill string vibrations that lead to large lateral displacements and subsequent impacts against the wellbore wall. Additionally, Santos et al. conclude that these drill string vibrations are particularly crucial as the leading cause of wellbore instability when drilling in hard rock formations (Santos et al., 1999).

In a study conducted by Placido et al. (2002), the influence of drill-string vibrations on wellbore instability was assessed across different wells (Placido et al., 2002). Vibrational events were tracked at the surface using metrics such as hook load, rotation speed, torque, and standpipe pressure. A detailed examination of these vibrational data with caliper logs revealed a strong link between instances of drill-string vibrations and wellbore enlargement. Interestingly, even though the lithological features of two wells were almost the same, their wellbore stability profiles differed. The first well displayed intense vibrational activity and featured numerous areas where significant

* Corresponding author's e-mail address: hadi.haghgouei@ntnu.no

wellbore enlargement occurred, making it markedly unstable. In contrast, the second well, characterized by moderate drill string vibrations, maintained relative wellbore stability. Moreover, shale formations did not show increased instability when water-based drilling fluids were used. The most significant instability was observed in the diabase layers, suggesting that drill string impacts, rather than physicochemical interactions between the rock and the drilling fluid, were the primary drivers of wellbore instability.

Zhu and Liu (2013) introduced a framework for assessing a single impact of drill string and its interactions with the wellbore wall (Zhu and Liu, 2013), drawing on experimental data and numerical simulations using the commercial software Abaqus. The study delves into the calculation of rock fragmentation in the wellbore resulting from drill string impacts, exploring the interrelationships under varying conditions such as contact length of the drill string, impact velocity, and rotational speed. Additionally, they derive equations for determining the critical speed of the drill string and the volume of rock fragments, based on both laboratory investigations and computational simulations**.**

Khaled (2017) stated that there exists a direct correlation between the initiation of whirl vibrations and wellbore instability. By considering some simple analytical formulation, Khaled concluded that when a vibrating drill string comes into contact with the wellbore wall, collapse is likely due to factors such as compressive failure of the rock, rock fatigue, and diminished rock strength (Khaled, 2017).

Lenwoue et al. (2022) explored the effects of cyclic loads induced by drill string vibrations on the evolution of natural fractures in the near-well rock (Kamgue Lenwoue et al., 2021; Lenwoue et al., 2022). Utilizing the cohesive zone element in the Abaqus commercial software for their numerical analysis, they found that the profile of fracture width over time exhibited a sinusoidal pattern, mirroring the cyclic load profiles of drill string vibrations. The findings further indicate that both fracture width and lost-circulation rates were substantially affected by these drill string vibrations.

Ma et al. (2022) employed a finite element model to assess wellbore stability in horizontal wells, using Abaqus (Ma et al., 2022). The Normalized Yielded Zone Area (NYZA) was used as a metric for evaluating wellbore stability. Their simulations demonstrated that the NYZA undergoes evolution in three distinct phases: static balance, dynamic growth, and dynamic balance. The results suggested that the initial collision of the drill string primarily influences wellbore stability. Additional findings indicate that both lateral acceleration and friction effects play a significant role in wellbore stability. Factors such as the initial collision position and the size of the drilling tool were found to have some influence on stability, while the rotational speed of the drill string was observed to have minimal effect.

It becomes evident that there is a significant research gap concerning the study of wellbore instability induced by drill string vibrations, particularly in the context of repetitive or cyclic impacts. The phenomenon of rock fatigue due to cyclic loading by the drill string vibration remains underexplored. While fatigue—the progressive reduction in material strength under sub-ultimate-strength loading—is a well-recognized failure mechanism in rocks, the bulk of existing research predominantly focuses on experimental observations. The phenomenon of fatigue induced by drilling processes and vibrations is complex (Dunayevsky et al., 1993) and requires rigorous investigation through numerical analysis. One of the primary challenges in numerically modeling rock fatigue is the lack of an appropriate constitutive model that can accurately capture the degradation of material strength under repetitive loading. To close this gap, the objective of this paper is to present a numerical model that was developed to evaluate rock fatigue during drilling processes, specifically resulting from lateral vibrations of the drill string. The Drucker-Prager elasto-plastic model with nonlinear hardening was utilized as the foundational framework for the computational analysis. Additionally, coupled damage model was proposed to mimic material strength degradation under cyclic loading. This customized elastic-plastic model, combined with the proposed coupled damage model, was implemented as a user-defined subroutine in Abaqus. Through this approach, wellbore instability associated with lateral drill string vibrations was examined.

2. Constitutive modeling of rock

2.1. Elasto-plastic model

One of the most well-known constitutive models in plasticity is the von Mises model. However, the von Mises model does not consider the pressure term in its equation, making it unsuitable for materials like soil and rock, which are pressure-sensitive. In contrast, the Mohr-Coulomb and Drucker-Prager constitutive models are notable for their pressure-dependent characteristics. The Mohr-Coulomb criterion is predominantly utilized as the most common failure model in geotechnical engineering. Its robustness and the straightforward nature of determining its parameters through standard tests make it a reliable choice for engineers. In the Haigh-Westergaard stress space, the yield surface of the Mohr-Coulomb model takes on the form of a conical prism, with its deviatoric section resembling an irregular hexagon. The Drucker-Prager model, on the other hand, has a conical yield surface in stress space and presents as a circle in the deviatoric plane. Fig. 1 represents the Mohr-Coulomb and Drucker-Prager yield function in the Haigh–Westergaard stress space.

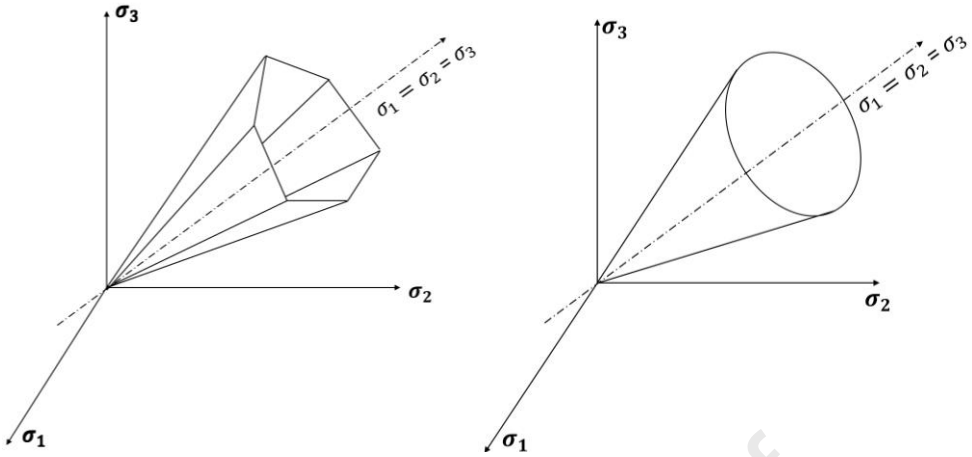

Fig. 1. The yield surface of (a) Mohr-Coulomb and (b) Drucker–Prager criterion in Haigh–Westergaard stress space.

The Mohr-Coulomb model implementation complexity arises from the presence of singular points on its hexagonal yield surface, whereas the Drucker-Prager model's failure surface is smooth and free of singularities, and it allows for more straightforward computational analysis due to its circular geometry in the deviatoric plane.

One of the benefits of the Mohr-Coulomb constitutive model is that its parameters can be easily determined from standard rock mechanical tests. Similarly, the Drucker-Prager constitutive model serves as an adaptation of the Mohr-Coulomb model, where the input parameters are straightforward to obtain from the Mohr-Coulomb model. The Drucker-Prager yield function is given by

$$\left.\begin{array}{c} \Phi(\boldsymbol{\sigma}, c) = \sqrt{J_2} + \alpha\frac{I_1}{3} - \xi c \\ J_2 = \frac{1}{3}(I_1^2 - 3I_2) \\ I_1 = \sigma_{ii} \\ I_2 = \frac{1}{2}\left(\sigma_{ii}\sigma_{jj} - \boldsymbol{\sigma}_{ij}\boldsymbol{\sigma}_{ij}\right) \end{array}\right\} \quad (1)$$

where c is the cohesion, α and ξ are Drucker-Prager model parametrs which can be determined through the calibration process for both the Drucker-Prager and Mohr-Coulomb models. I_1 and I_2 are the first and second invariant of the Cauchy stress tensor, $\boldsymbol{\sigma}_{ij}$, and J_2 is the second invariant of the deviatoric stress tensor, $\boldsymbol{s}_{ij}$.

There are multiple approaches for calibrating the Drucker-Prager yield surface in relation to the Mohr-Coulomb model, specifically in terms of defining the parameters α and ξ. The three most used methods are known as inner edge or extension, outer edge or compression, and plane strain failure calibration (de Souza Neto et al., 2011). The terms inner and outer edge describe how the Drucker-Prager yield surface fits with the Mohr-Coulomb yield surface edges. When visualized on the π-plane under a given mean stress, one can align the edges of the Mohr-Coulomb and Drucker-Prager yield surfaces either through the extension configuration or the compression configuration, where the Lode angle is $\theta = \pm\pi/6$. Fig. 2 illustrates both the inner and outer edge calibration techniques.

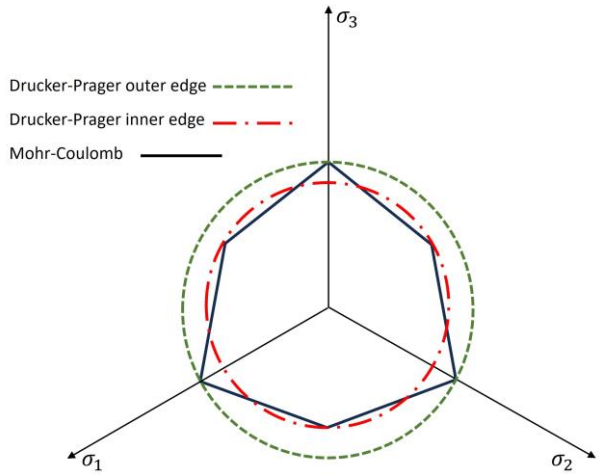

Fig. 2. The schematic representation of Mohr-Coulomb and Drucker-Prager yield surface in the π-plane.

If the calibration aims for both models to predict equivalent collapse loads under plane strain conditions, then the method is referred to as plane strain mode. The relationships between the Drucker-Prager and Mohr-Coulomb parameters based on the outer edge, inner edge, and plain strain approximation procedures are given by Eqs. (2a), (2b), and (2c) respectively (de Souza Neto et al., 2011):

$$\left.\begin{aligned}\alpha &= \frac{6\sin\varphi}{\sqrt{3}(3-\sin\varphi)}\\ \xi &= \frac{6\cos\varphi}{\sqrt{3}(3-\sin\varphi)}\end{aligned}\right\} \quad (2a)$$

$$\left.\begin{aligned}\alpha &= \frac{6\sin\varphi}{\sqrt{3}(3+\sin\varphi)}\\ \xi &= \frac{6\cos\phi}{\sqrt{3}(3+\sin\varphi)}\end{aligned}\right\} \quad (2b)$$

$$\left.\begin{aligned}\alpha &= \frac{3\tan\varphi}{\sqrt{9+12\tan^2\varphi}}\\ \xi &= \frac{3}{\sqrt{9+12\tan^2\varphi}}\end{aligned}\right\} \quad (2c)$$

where φ is internal friction angle. The apex of the yield surface of Drucker-Prager model aligns with that of the Mohr-Coulomb model. It should be noted that singularity exists at the apex of both the Mohr-Coulomb and Drucker-Prager yield surface.

It is established that within the framework of standard elastoplasticity, one may assume that the strain experienced by a material can be additively partitioned into elastic and plastic parts. The elastic component of the strain is typically derived from linear elastic constitutive equations, such as Hooke's law. Conversely, the computation of the plastic strain component requires the incorporation of both a flow rule and a hardening model. Flow rule indicates how strain will develop in plastic regime and the hardening rule describes the change of the yield surface under plastic deformation. To formulate the flow rule, it is crucial to initially acknowledge that the Drucker-Prager constitutive model has a singularity at the apex of the yield surface but is smooth elsewhere (de Souza Neto et al., 2011). As a result, consideration must be given to two distinct situations: plastic yielding on the smooth portions of the cone surface and plastic yielding at the apex.

2.1.1. Flow rule

Two primary categories of flow rules are discussed in the literature: associative and non-associative flow rule. In the case of associative flow rule, the rate of plastic strain is aligned with the gradient of the yield function, or equivalently, is perpendicular to the yield surface in the stress space. Thus, the direction of the plastic deformation coincides with the normal to the yield surface. For non-associative flow rule, the rate of plastic strain is not directly proportional to the gradient of the yield function but is instead aligned with the normal to another surface given by the 'plastic potential function'. This function dictates the direction of plastic flow within the stress space.

Studies have indicated that for geomaterials plastic deformation does not align with the normal to the yield surface so that associative flow rules are less suitable, especially failing to predict realistic dilation behavior (Cai et al., 2018). Therefore, this study will employ a non-associative flow rule for Drucker-Prager model by considering the parameter $\bar{\alpha}$, which depends on the dilatancy angle, ψ. The plastic potential is described by

$$\Omega(\boldsymbol{\sigma}) = \sqrt{J_2} + \bar{\alpha}\frac{I_1}{3} \quad (3)$$

Depending on the Drucker-Prager approximation chosen to represent the Mohr-Coulomb model, $\bar{\alpha}$ can be determined for outer edge, inner edge, and plane strain compatibility, from Eqs. (4a), (4b), and (4c), respectively:

$$\bar{\alpha} = \frac{6\sin\psi}{\sqrt{3}(3-\sin\psi)} \quad (4a)$$

$$\bar{\alpha} = \frac{6\sin\psi}{\sqrt{3}(3+\sin\psi)} \quad (4b)$$

$$\bar{\alpha} = \frac{3\tan\psi}{\sqrt{9+12\tan^2\psi}} \quad (4c)$$

By differentiating Eq. (3) with respect to stress tensor, it is possible to find the vector normal to the potential function surface and thereby to find the non-associative flow rule for the Drucker-Prager model on the smooth surface. The flow rule for the smooth portion of the yield surface is described by:

$$\dot{\varepsilon}^p = \dot{\gamma}\boldsymbol{N} \quad (5)$$

where $\boldsymbol{N}$ is the flow vector, γ is the scaler plastic multiplier, and the dot represents time derivative.

The flow vector, $\boldsymbol{N}$, can be found on the smooth portion of the yield surface as follows:

$$\boldsymbol{N} = \frac{\partial\Omega}{\partial\boldsymbol{\sigma}} = \frac{1}{2\sqrt{J_2}}\boldsymbol{s}_{\mathrm{ij}} + \frac{\bar{\alpha}}{3}\delta_{\mathrm{ij}} \quad (6)$$

where δ_{ij} is the Kronecker delta. At the apex of the yield surface, the potential function is not differentiable, and the flow vector therefore is the sub-gradient of the potential function (de Souza Neto et al., 2011).

The accumulated plastic strain on the smooth surface can be obtained using

$$\dot{\varepsilon}^p = \dot{\gamma}\xi \quad (7)$$

where $\dot{\varepsilon}^{\mathrm{p}}$ is the rate of the accumulated plastic strain. For the apex of the yield surface, the following equation should be used:

$$\dot{\varepsilon}^p = \frac{\xi}{\bar{\alpha}}\dot{\varepsilon}_{\mathrm{v}}^{\mathrm{p}} \quad (8)$$

where $\dot{\varepsilon}_{\mathrm{v}}^{p}$ is the rate of volumetric plastic strain.

2.1.2. Hardening

To mimic how the material strength is changing as plastic strain accumulates, a hardening law is assumed in terms of a scalar thermodynamic force H as a function of the accumulated plastic strain $H = H(\bar{\varepsilon}^{\mathrm{p}})$ as follows:

$$\sigma_y(\bar{\varepsilon}^{\mathrm{p}}) = \sigma_{y_0} + H(\bar{\varepsilon}^{\mathrm{p}}) \quad (9)$$

where σ_{y_0} is the initial yield strength of the material and H is a scalar thermodynamic force. In geomaterials, it is suitable to consider the cohesion as a fundamental strength parameter or an internal variable in the hardening law:

$$c = c(\bar{\varepsilon}^{\mathrm{p}}) \quad (10)$$

This assumption will be adopted in this study.

2.2. Damage model

Fatigue is characterized as the progressive evolution of the failure of a material subjected to cyclic loading, even at stress levels below the ultimate strength (Haghgouei et al., 2021; Alizadeh et al., 2023). Previous experimental studies indicated that repetitive loading leads to a gradual reduction in the rock strength, ultimately leading to fatigue failure (Haghgouei et al., 2018). A significant challenge in the application of numerical models to fatigue failure is having access to constitutive models that can account for the material degradation during mechanical loading. One approach to modeling this decay in the material strength involves the use of cohesive zone elements, as demonstrated by Lenwoue et al. (2022). However, this approach requires the predefined fracture growth paths and the incorporation of cohesive elements along these paths.

Another potential solution is to employ a damage model. Unfortunately, existing damage models in commercial software are generally inadequate for simulating fatigue under cyclic loading, especially when dealing with geomaterials under constant amplitude loading conditions. Existing research indicates that under constant cyclic loading within a given stress range, damage will grow solely during the first cycle. Subsequent cycles do not exhibit additional damage unless the stress amplitude exceeds that of the initial level (Bao et al., 2011; Chen et al., 2022).

To overcome this limitation, this study describes the development and implementation of a new damage model within the Abaqus simulation environment. Distinguished by its coupled damage mechanics, the model is designed to work closely with plasticity equations. This coordinated approach enables a more precise capture of how the material's strength degrades under conditions of cyclic loading.

Wang et al (2016) reported that the change in plastic strain of rocks subjected to cyclic loading has three stages, the initial or deacceleration stage, the steady stage, and finally the accelerated stage (Wang et al., 2016) as seen in Fig. 3.

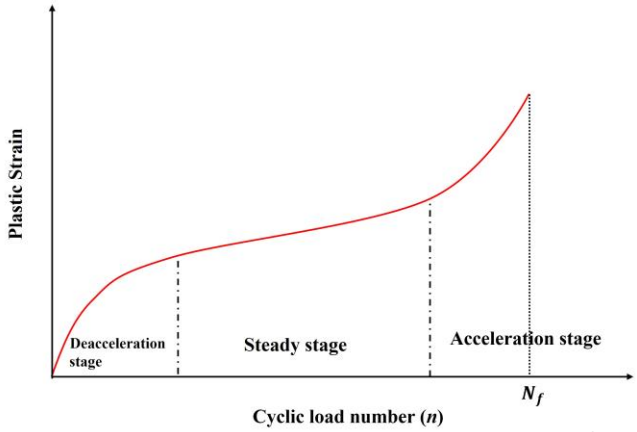

Fig. 3. Plastic strain development in rocks under cyclic loading.

To capture this phenomenological behavior the following damage model is proposed,

$$\left.\begin{array}{l} D = \frac{\sigma_{\mathrm{m}}^{\mathrm{t}}}{\sigma_{\mathrm{m}}^{\max}}\left(a + b\ln\left(\frac{x}{1-x}\right)\right) \\ x = \frac{n}{N_{\mathrm{f}}} \quad x\epsilon(0,1) \end{array}\right\} \qquad (11)$$

where D stands for damage, a and b are constant parameters, n is the number of cycles experienced by the material and N_f is the number of cycles to failure. $\sigma_{\mathrm{m}}^{\mathrm{t}}$ and $\sigma_{\mathrm{m}}^{\max}$ denote the current and maximum mean stress value, respectively. The parameter x cannot take the values of 0 and 1, as these values would make Eq. (11) singular. This has a physical meaning where the value of $x = 0$ corresponds to static loading, where cyclic loading has not yet started. Meanwhile, $x = 1$ would represent the case where complete failure has occurred, which is beyond the scope in our fatigue studies. The rate at which the equation approaches singularity, i.e. when x is close to 0 or 1, is controlled by the constants a and b.

In continuum damage mechanics, the concept of effective stress for damage is employed. This means that the actual stress is replaced with an effective stress that takes into account a damage parameter (D). In the context of continuum damage mechanics, this is described by

$$\boldsymbol{\sigma}_{effective} = \frac{\boldsymbol{\sigma}}{1-D} \quad (12)$$

As can be seen in Eq. (12), when the damage D approaches 1.0, the effective stress tends towards infinity, which is not physically meaningful, and values larger than 1.0 yield negative stresses. Therefore, the critical damage value must be below 1.0.

This proposed damage model will be coupled to our elasto-plastic model.

2.3. Integration algorithm

To determine the stress tensor for each finite element, the following integration algorithm is applied where the trial stress tensor following a linear elastic law is given by

$$\sigma_{n+1} = \sigma_{n+1}^{\mathrm{trial}} - \Delta\gamma \mathrm{E}^{e} N_{\mathrm{n+1}} \quad (13)$$

where E^{e} is the elasticity matrix. The subscript $n+1$ represents the next increment, and the superscript 'trial' indicates the initial prediction of stress based on the elastic condition. The second part on the right-hand side of Eq. (13), i.e. $\Delta\gamma \mathrm{E}^{e} N_{n+1}$, is the return vector(de Souza Neto et al., 2011). When the plasticity condition is met, the predicted elastic stress is corrected to its true value using the return mapping algorithm. The return mapping algorithm acts as a computational technique for ensuring that the key equations and yield conditions are met during the plastic deformation. This method modifies the internal factors, including stress and plastic strains, to represent the material's new state after experiencing plastic deformation. Usually, this consists of a series of iterative steps that begin with a preliminary stress status and then recalibrate the stress to conform to the yield surface, all while adjusting other internal variables based on the plastic constitutive model. The flow vector N is different for smooth and apex parts of the Drucker-Prager model (de Souza Neto et al., 2011). In the following subsection, the return to each portion will be examined.

2.3.1. Return to smooth part of yield surface

The change in the plastic strain can be defined as follows:

$$\Delta\varepsilon^{p} = \Delta\gamma N_{n+1} = \Delta\gamma\left(\frac{1}{2\sqrt{J_2}}s_{\mathrm{ij}\,n+1} + \frac{\bar{\alpha}}{3}\delta_{\mathrm{ij}}\right) \quad (14)$$

Eq. (13) and Hooke's law yield

$$\sigma_{n+1} = \sigma_{\mathrm{n+1}}^{\mathrm{trial}} - \Delta\gamma\left(\frac{G}{\sqrt{J_2}}s_{\mathrm{ij}\,n+1}^{\mathrm{trial}} + \frac{K\bar{\alpha}}{3}\delta_{\mathrm{ij}}\right) \quad (15)$$

where K and G are the bulk and shear modulus respectively. During plastic deformation, the consistency condition assures that the stress state is on the yield surface. The consistency condition is given by

$$\Phi_{n+1} = \sqrt{J_2} + \alpha\frac{I_{1\,n+1}}{3} - \xi c\left(\bar{\varepsilon}_{n+1}^{\mathrm{p}}\right) = 0 \quad (16)$$

where the next increment of the accumulated plastic strain is given by

$$\left.\begin{aligned}\bar{\varepsilon}_{n+1}^{\mathrm{p}} &= \bar{\varepsilon}_{n}^{\mathrm{p}} + \Delta\bar{\varepsilon}^{\mathrm{p}}\\ \Delta\bar{\varepsilon}^{p} &= \xi\Delta\gamma\end{aligned}\right\} \quad (17)$$

By considering the consistency condition, the following nonlinear equation for Δγ is obtained:

$$\sqrt{J_2^{\mathrm{trial}}} - G\Delta\gamma + \alpha\left(\frac{I_{1\,n+1}^{\mathrm{trial}}}{3} - K\bar{\alpha}\Delta\gamma\right) - \xi c\left(\bar{\varepsilon}_{n}^{\mathrm{p}} + \xi\Delta\gamma\right) = 0 \quad (18)$$

2.3.2. Return to apex of yield surface

The consistency condition on the apex of the yield surface can be expressed as

$$c\left(\bar{\varepsilon}_{n}^{\mathrm{p}} + \Delta\bar{\varepsilon}^{\mathrm{p}}\right)\frac{\xi}{\alpha} - \frac{I_{1\,n+1}^{\mathrm{trial}}}{3} + K\Delta\varepsilon_{\mathrm{v}}^{\mathrm{p}} = 0 \quad (19)$$

The return mapping equation for the singularity point at the apex of the yield surface is given by

$$c\left(\bar{\varepsilon}_{n}^{\mathrm{p}} + \frac{\xi}{\bar{\alpha}}\Delta\varepsilon_{\mathrm{v}}^{\mathrm{p}}\right)\frac{\xi}{\alpha} - \frac{I_{1\,n+1}^{\mathrm{trial}}}{3} + K\Delta\varepsilon_{\mathrm{v}}^{\mathrm{p}} = 0 \quad (20)$$

The plastic strain and stress are updated using (de Souza Neto et al., 2011):

$$\left.\begin{aligned}\bar{\varepsilon}_{n+1}^{p} &= \bar{\varepsilon}_{n}^{\mathrm{p}} + \frac{\xi}{\alpha}\Delta\varepsilon_{\mathrm{v}}^{\mathrm{p}}\\ \sigma_{n+1} &= \left(\frac{I_{1\,n+1}^{\mathrm{trial}}}{3} - K\Delta\varepsilon_{\mathrm{v}}^{\mathrm{p}}\right)\delta_{\mathrm{ij}}\end{aligned}\right\} \quad (21)$$

In the implementation that we have presented here, the elastic stress is initially calculated at time t_n based on Hooke's law. Following the calculated stress field, the plastic condition is estimated based on the calculated stress state. If the stress remains within the elastic regime, i.e. the stresses are within the yield surface, then the elastic stress is considered accurate for this time increment t_n, and the calculation proceeds to find the stress at time t_{n+1}. If, however, the plastic condition is met, a return-mapping algorithm is used to satisfy the consistency condition for plasticity. In this situation, the Newton-Raphson iterative method is employed to determine $\Delta\gamma$. During the iterative scheme convergence is analyzed, and if convergence is achieved, and the result falls within the prescribed tolerance level, the stress field is updated. This updated stress field is then verified to determine whether the return-mapping on the smooth portion of the yield surface is accurate. If it is, then the solution is considered correct, and the calculations can begin for the next time increment. If the return-mapping on the smooth portion is invalid, consideration is given to the return-mapping at the apex of the yield surface, and the Newton-Raphson method is employed to find the volumetric plastic strain. When convergence is confirmed, the stress field is updated. The flow chart presented in Fig. 4 illustrates the solution procedure.

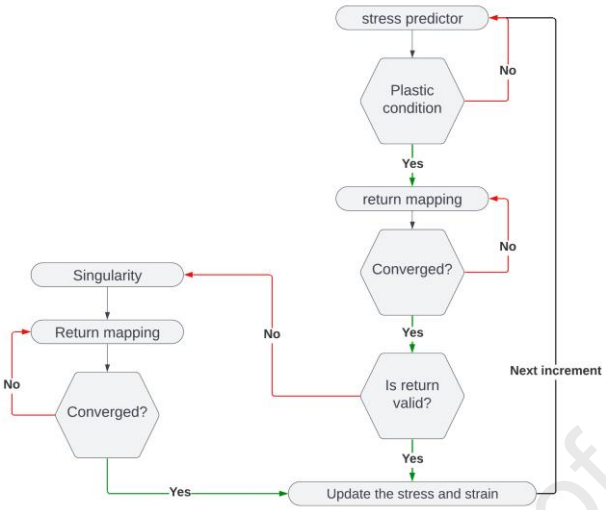

Fig. 4. Flow Chart of Elasto-Plastic Computational Framework.

The aforementioned model was implemented into a user-defined Fortran subroutine. This was combined with the Abaqus explicit solver, and the problem of drill string vibration-induced fatigue was simulated.

3. Verification of elasto-plastic damage model with wellbore stability experiment

In the previous section, the elasto-plastic damage model was introduced. To validate the accuracy of the model in predicting wellbore failure under the impact of a drill string, it will be verified using experiment conducted by Zhu and Liu (2013).

Zhu and Liu (2013) studied the impact on wellbore walls, with a specific focus on rock fragmentation. They considered a quarter of the wellbore in their experiment and used a steel sphere as an impactor.

A 3D finite element model was employed in our study to recreate the experiment conducted by Zhu and Liu (2013) through numerical simulation. The model was constructed using a total of 214,215 elements, with the element type designated as C3D8 (eight-node linear brick). Nodal contact was established between the steel sphere (imitating a drill string) and the rock formation. The penalty contact formulation was used, and a friction angle of 0.4 was set for tangential behavior during contact. The hard contact type was chosen for pressure-overclosure behavior, and the simulation permitted separation of the steel sphere from the wellbore wall after contact. The external boundary of the model was fixed in terms of displacement in the normal direction. The numerical model is illustrated in Fig. 5.

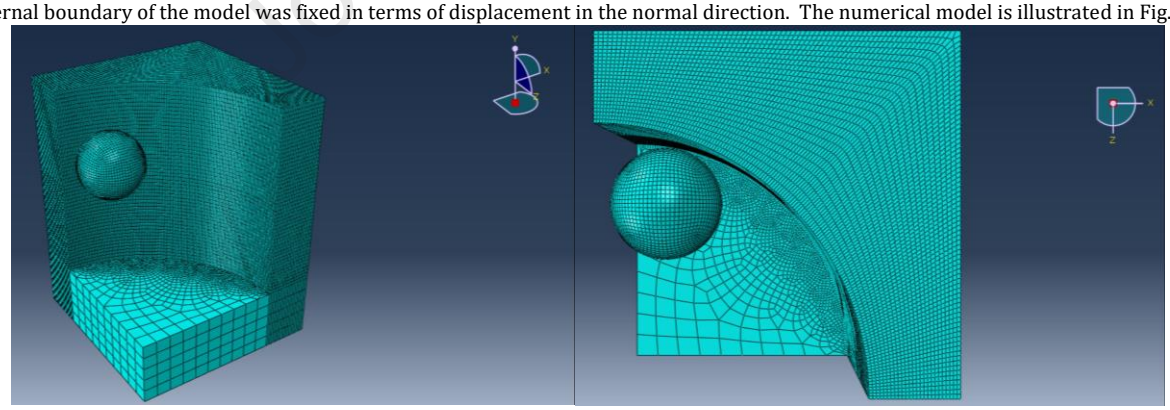

(a) (b)

Fig. 5. The geometry of the finite-element model: (a) front view and (b) top view.

Zhu and Liu (2013) reported that with an initial velocity of 4.1 m/s, the residual or rebound velocity of the steel sphere in the experiment was 0.0943 m/s. This data is utilized to calibrate the elasto-plastic model in the present study. The mechanical properties of the rock and steel sphere used in the numerical model were sourced from Zhu and Liu's (2013) work. The elastoplastic behavior of the rock is crucial when comparing initial and residual velocities in impact problems. The ratio of residual to initial velocity in impact problems is termed the restitution coefficient defined as

$$e = -\frac{v_r}{v_i} \quad (22)$$

where v_r and v_i are the residual and initial velocity, respectively. By considering the conservation of momentum during the impact, the restitution coefficient can be expressed as follows:

$$e^2 = \frac{K_r - K_c}{K_i - K_c} \leq 1 \quad (23)$$

where K_r, K_c, and K_i are the residual, contact time, and initial kinetic energy, respectively.

Based on Eq. (23), when $e = 1$, K_i is equal to K_r. In this case, the kinetic energy is conserved, indicating an elastic impact. This suggests that internal responses within the body, such as vibrations, are negligible and no energy will dissipate. After such an impact, the body returns to its original form without any energy loss.

Considering Eq. (23) when $e = 0$, it follows that $K_r = K_c$, characterizing the impact as purely plastic. This suggests that the impact concludes at $t = t_c$, which corresponds to the moment the impactor contacts the target. During this interaction, energy is lost. The loss of kinetic energy results in plastic deformation of the bodies, and this plastic work dissipates as heat. For any other values of e, within the range $0 < e < 1$, the impact is elasto-plastic, indicating that the bodies experience some permanent deformation, albeit less than in a purely plastic scenario (Menčík, 2018). Consequently, as highlighted, the restitution coefficient and the residual velocity are greatly influenced by the elasto-plastic behavior of the material. However, Zhu and Liu (2013) did not furnish a stress-strain curve or details on the hardening parameter. Therefore, in this study, a Python script was developed to iteratively adjust the hardening parameters to achieve the calibration goal: a residual velocity of 0.0943 m/s.

From a numerical point of view, failure can be simulated by setting the integration point value in the element to zero and then removing these elements to visualize failure. This method is known as element deletion or the erosion technique (Belytschko et al., 2014). The fragmentation of rock is achieved by employing this technique. The failure criterion is based on the plastic strain at failure, ε_f^p, as described by Zhu and Liu (2013). Fig. 6 illustrates the radial velocity of the steel sphere throughout the simulation. The initial velocity is 4.1 m/s, and the residual velocity is 0.0944 m/s, which aligns well with the findings of Zhu and Liu (2013).

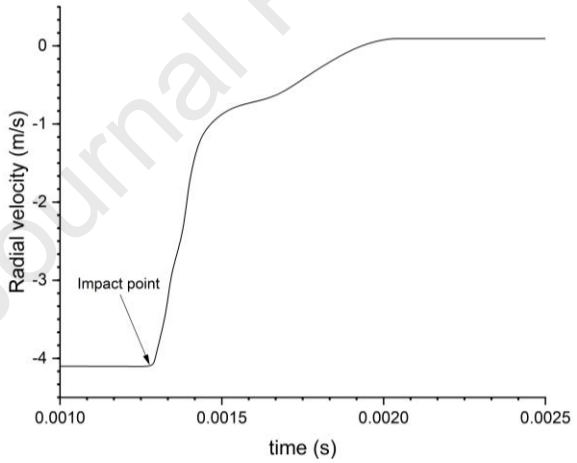

Fig. 6. The change of radial velocity during the impact of steel sphere on the wall of the wellbore.

After calibrating the hardening parameter, the validation of the calibrated model was conducted by considering different initial velocities of the steel sphere. This comparison is listed in Table 1. In this table v_r is the initial velocity and v_r^{exp} and v_r^{num} are the residual velocity from the experiment conducted by Zhu and Liu (2013) and the residual velocity from our numerical simulation, respectively.

Table 1.

Comparison of radial velocity between numerical simulation and experimental data.

v_i(m/s)	v_r^{exp}(m/s)	v_r^{num}(m/s)	Relative error (%)
3.5	0.87	0.91	4.6
3.8	0.38	0.4	5.2
4.4	0.136	0.131	3.6

As evident from Table 1, the elasto-plastic model is adept at evaluating wellbore failure caused by the steel sphere's collision with the wellbore wall. Fig. 7 illustrates the wellbore wall failure after impact of steel sphere with the initial velocities of 4.1 m/s and 4.4 m/s.

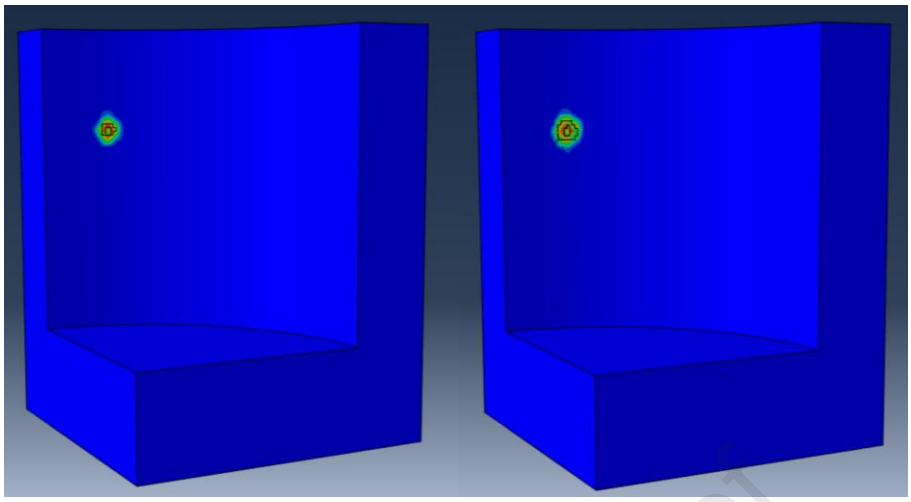

(a) (b)

Fig. 7. Rock failure on the wall of the wellbore due to steel sphere impact with the initial velocity of (a) 4.1 m/s and (b) 4.4 m/s.

4. Numerical investigation of wellbore failure under repetitive impact of drill string

In the preceding section, the proposed model was validated against experimental data. This section aims to use the elasto-plastic damage model to explore the impact of drill string vibration on wellbore stability.

A 2D plain strain finite element model (FEM) was employed, featuring a wellbore with a radius of 0.2159 m. The rock formation was modeled as a square block with side dimensions of 2 m. Material properties are detailed in Table 2.

Table 2. The material properties and convergence tolerance used in numerical simulations.

Parameter	Density(kg/m^3)	E(GPa)	ν	c(MPa)	φ ($^\circ$)	ψ (degree)	ξ	α	$\bar{\alpha}$	Convergence tolerance
Value	2700	30	0.3	7	40	20	0.72	0.60	0.33	0.001

Since the primary objective of this study was to introduce the elasto-plastic coupled damage model for investigating wellbore fatigue failure, the effect of pore pressure was neglected in the model.

The elements used for the rock formation were of type CPE4 (four-node plane strain quadrilateral element). Mesh refinement was used near the wellbore to enhance the accuracy. The total number of elements in the model was 71,653. The geometric layout of the model with mesh is shown in Fig. 8.

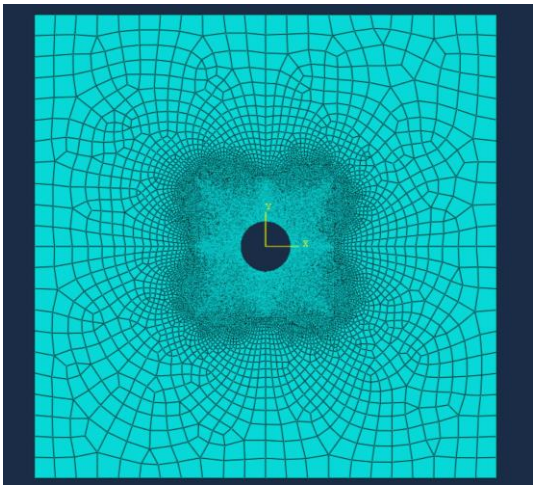

Fig. 8. The geometry and mesh of the numerical model.

The solution procedure consisted of two steps. Initially, to establish the geostatic conditions, the model was simulated without incorporating drill string vibrational loads. To mitigate the effects of boundary load on the shape of rock failure, hydrostatic conditions were assumed. Upon solving this preliminary model, all displacements were set to zero.

In the second step, drill string vibrations were introduced. The diameter of the drill string was 127 mm. The loading of the drill string was directed at a random azimuth around the wellbore. The loading was generated using a user-defined Fortran subroutine, VDLOAD, as input to the Abaqus solver. The VDLOAD subroutine was designed to generate loading-unloading over a predefined time-period to model the impact of the drill string onto the wellbore as a pressure load with the maximum magnitude of 40 MPa. The loading-unloading period, representing the time for one impact, was 10 ms, 5 ms to load and 5 ms to unload. Each drill string impact on the wellbore wall occurred at a random azimuth, and the contact length between the drill string and the borehole wall was around 9.398 mm. In this study the total generated impact will refer to total impacts. It should be noted that this is the cumulative number of impacts during simulation, and individual parts of the wellbore wall experienced fewer impacts.

To identify potential instability in the solution of a nonlinear problem, it is crucial to monitor the energy balance during explicit FEM analysis. Such instabilities can result in spurious energy generation, thereby violating the law of energy conservation. For this, calculating the work done by both internal and external forces, as well as the kinetic energy in the finite element model, is necessary (Belytschko et al., 2014). Energy conservation was monitored throughout the simulation, and the simulation would be terminated if any violations occurred.

In the simulations presented in this paper, the critical damage value at which the rock will fail was set to 0.9. The damage function parameters used in the current study are given in Table 3.

Table 3

Damage parameters used in the simulation.

Parameter	a	b	N_f
Value	0.6	0.09	70

In this study when the damage value reached the critical value, i.e. 0.9, the element was deleted from the simulation and thereby rock failure could be observed.

The material's constitutive model, introduced in Section 2, was integrated into the Abaqus solver using another user-defined Fortran subroutine, VUMAT. The problem was subsequently solved using the Abaqus explicit solver.

5. Results

A plot depicting the evolution of equivalent plastic strain during the analysis is shown in Fig. 9 and the corresponding von Mises stress distribution in the model is shown in Fig. 10. To enhance the observation of stress concentration around the wellbore at the conclusion of the simulation, Fig. 11 displays a magnified view of Fig. 10i.

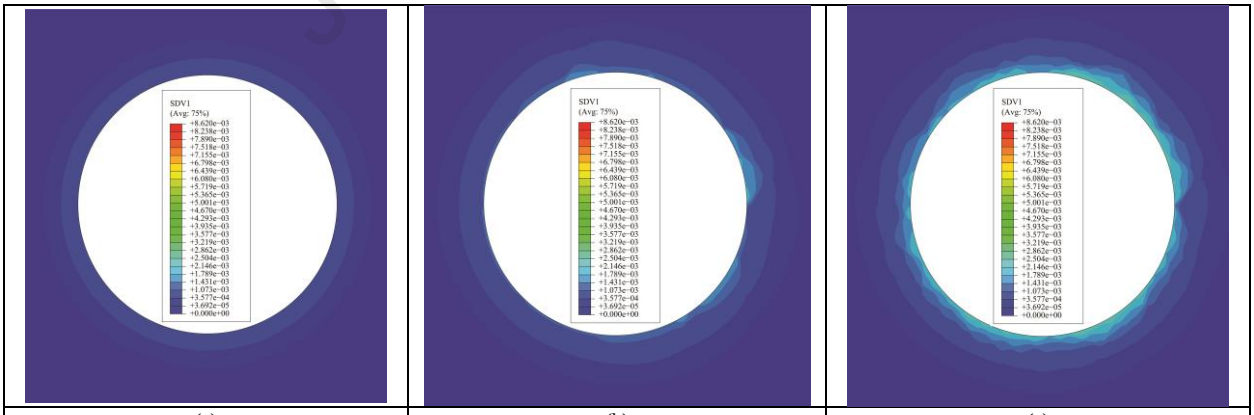

(a) (b) (c)

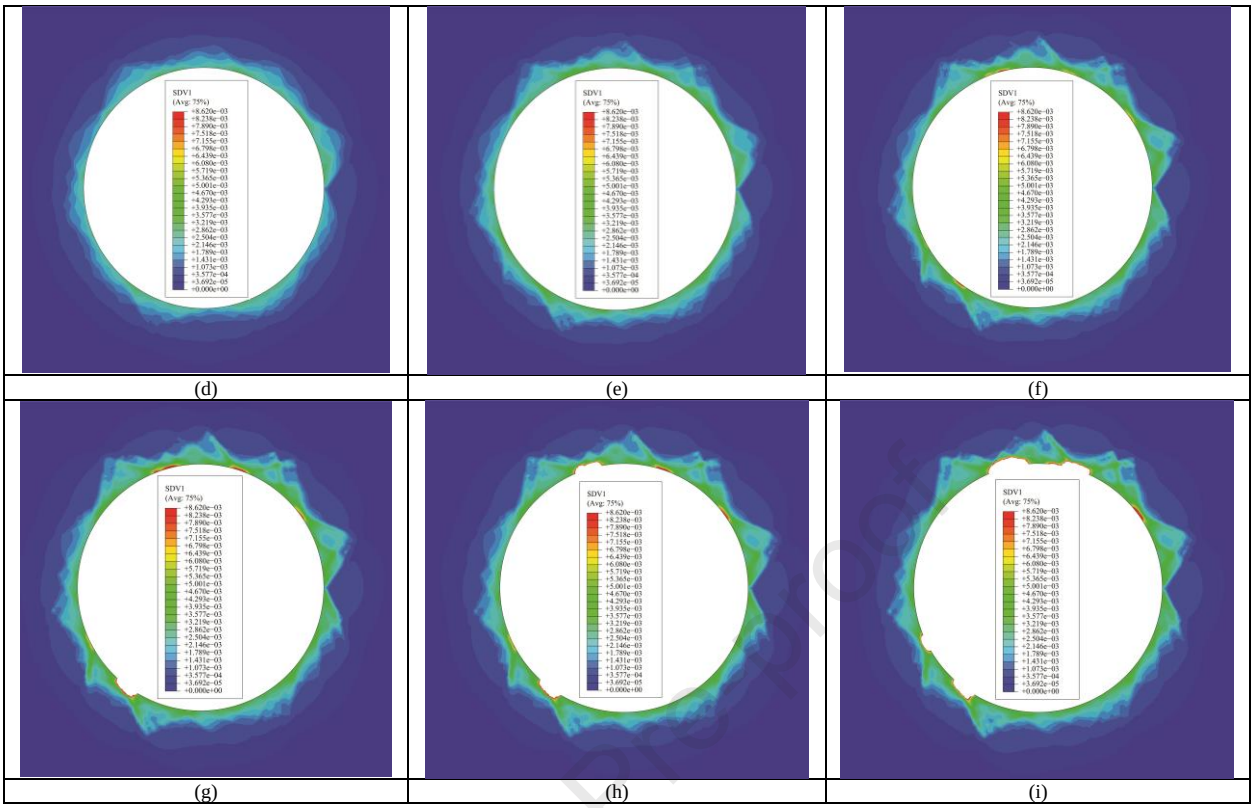

Fig. 9. The contour plot showing the development of plastic strain during simulation at: (a) $t = 0$ ms, (b) $t = 100$ ms, (c) $t = 500$ ms, (d) $t = 1000$ ms, (e) $t = 2000$ ms, (f) $t = 2600$ ms, (g) $t = 2820$ ms, (h) $t = 2850$ ms, and (i) $t = 2960$ ms. SDV1 (Solution Dependent state Variable 1) stands for equivalent plastic strain.

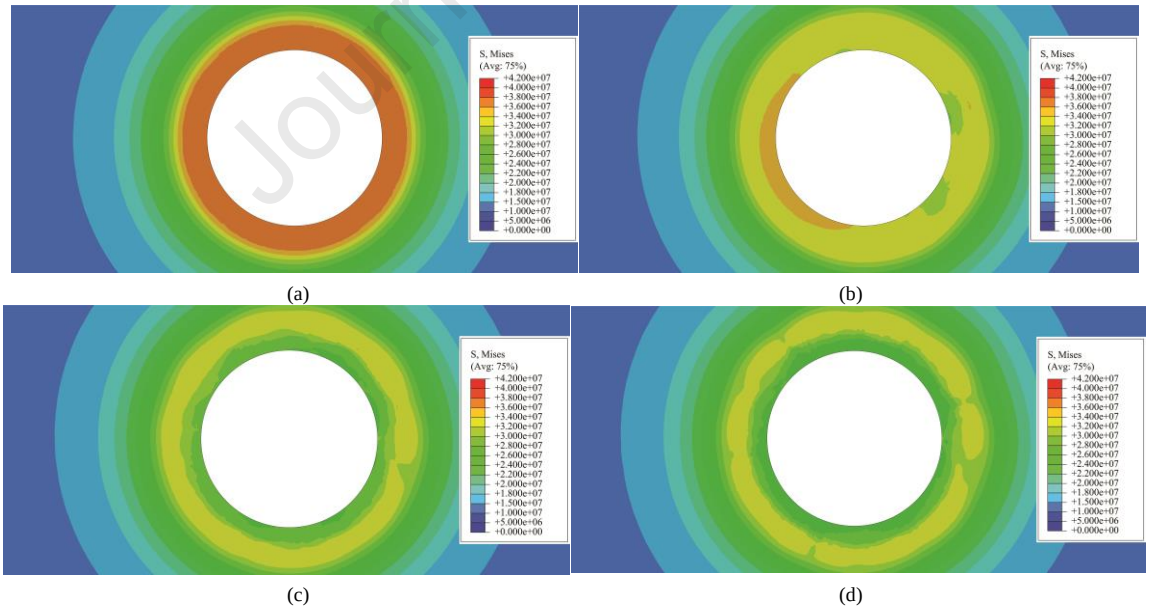

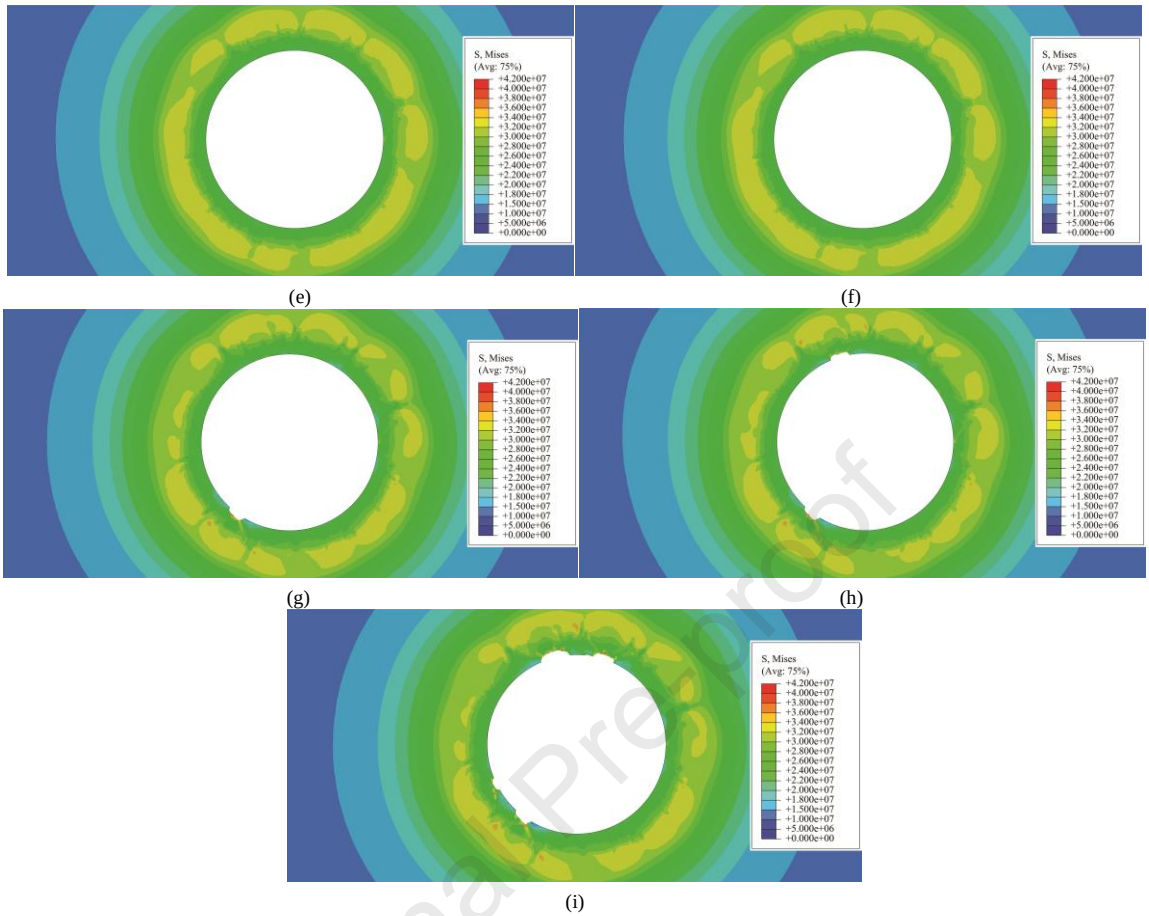

Fig. 10. The contour plot showing the distribution of von Mises stress around the wellbore during simulation at: (a) $t = 0$ ms, (b) $t = 100$ ms, (c) $t = 500$ ms, (d) $t = 1000$ ms, (e) $t = 2000$ ms, (f) $t = 2600$ ms, (g) $t = 2820$ ms, (h) $t = 2850$ ms, and (i) $t = 2960$ ms.

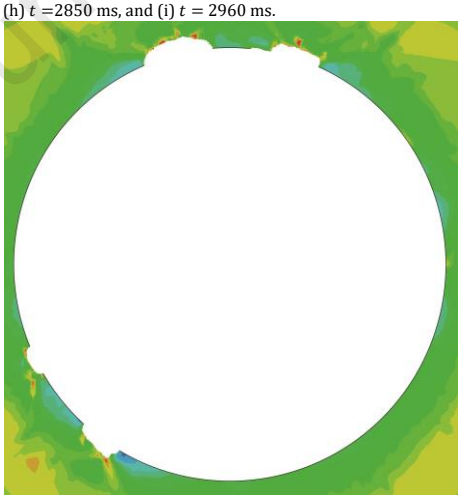

Fig. 11. The magnified view of Fig. 10i representing the stress concentration around the wellbore.

As the simulation time increases, the drill string repeatedly impacts the wall of the wellbore, leading to an increase in the equivalent plastic strain. This phenomenon is evident in Fig. 12 where damage and plastic strain evolution is shown for one of the elements on the top of the wellbore boundary for $t = 0$ to $t = 2000$ ms (200 impacts).

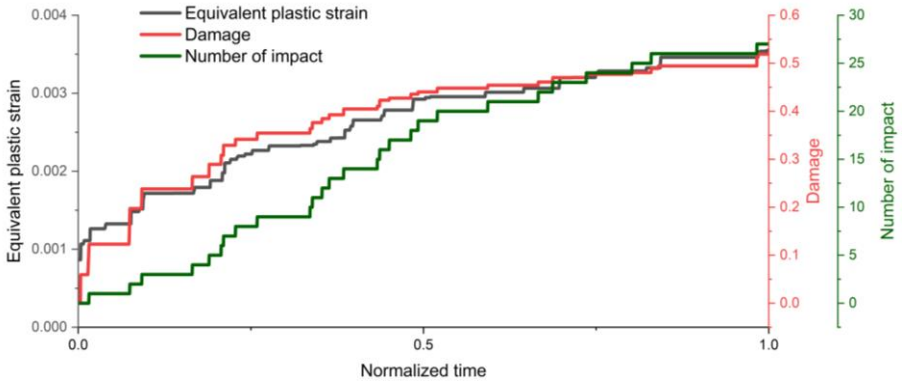

Fig. 12. Evolution of the plastic strain and damage parameter in the element on top side of the wellbore.

With each successive impact, damage increases, and consequently plastic strain increase is observed. This consistent pattern confirms the efficacy of the damage model, highlighting its capacity to effectively calculate the drill string vibration-induced fatigue of the rock formation through numerical analysis. The failure of rock can be seen in Fig. 9g to 9i. The example simulation was terminated at a time of 2960 ms, because after that point the model was not reliable, and the solution violated the energy conservation law. The cumulative impact count by the end of the simulation was 296, while the largest impact number experienced by a section of the wellbore was 62 impacts.

6. Discussion

The failure location is in this study dictated by the number of impacts and the damage value along the perimeter of the wellbore. Fig. 13 illustrates the number of impacts around the wellbore over time. As plastic strain is accumulated, the material strength is systematically deteriorated, and once the given threshold is reached, the material is removed. As may be seen from Fig. 9 and 13, the location of failure around the wellbore is influenced by the number of impacts, and randomness is included in the simulation by the location of the drill string hits.

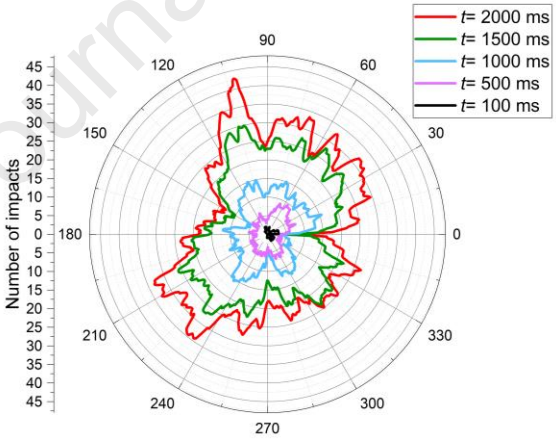

Fig. 13. The number of impacts during the time of simulation at different locations on the boundary of the wellbore; the outermost circle represents 45 impacts.

In the following, the model results during material damage until failure will be discussed, followed by a discussion on the simulations after the occurrence of failure – where rock fragments are removed from the borehole wall.

6.1. Plastic behavior prior to failure

The model results during damage development up to failure are discussed here. Being able to predict failure before it occurs would represent large gains during drilling. Having the possibility to avoid operational issues related to stuck-pipe and excessive cuttings transport is highly valued. The presented numerical model is intended to describe this phenomenon during drilling-operations. To simulate the onset of failure, the progressive damage is used to calculate rock deterioration, and when the damage parameter reaches a critical value of 0.9 the rock fails. In the model case presented here, rock failure initiated after the 280 total impacts (i.e. 2800 ms).

During wellbore stability investigations, engineers frequently neglect the effects of drill string impacts, mainly because of lack of objective information (i.e. both basic data and data analysis tools). Instead, wellbore stability assessments are typically focused on either a static stress state or fluctuations in the fluid pressure within the wellbore (Lenwoue et al., 2022). Fig. 14 illustrates the equivalent plastic strain distribution around the wellbore at the beginning of simulation (i.e. at the static balance) and just prior to rock failure. This picture may be compared to the number of impacts in Fig. 13. There is a significant difference between the equivalent plastic strain levels at the beginning of the simulation and those observed just before failure. This difference highlights the vital importance of incorporating the damage induced by drill string vibration into wellbore stability analyses.

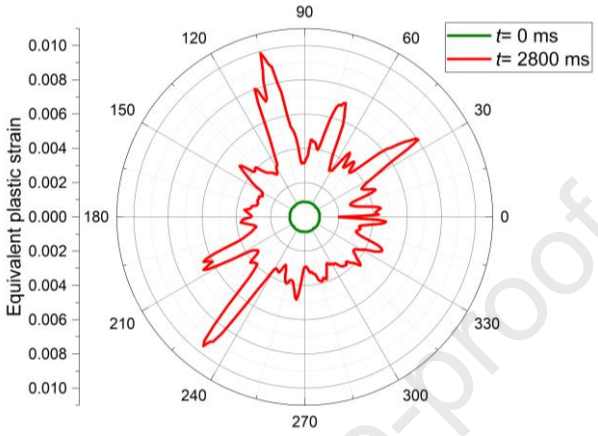

Fig. 14. Plastic strain development around the wellbore.

The effect of repetitive impact is not limited to the magnitude of plastic strain. The radius of the yielded zone around the wellbore is also strongly affected by drill string impacts. In Fig. 15, the equivalent plastic strain profile is shown along the path in the upper part of the wellbore (shown by the arrow). Five profiles are displayed, from $t = 0$ (before any hits) to 280 hits, just before failure occurs. As can be seen, there is plastic strain at initiation of the model due to geostatic condition (can be seen also in Fig. 9a), and its magnitude grows successively over time. The radius of the yielded zone along this specific path increases by 55 percent from the initiation of the model, and the peak equivalent plastic strain at the borehole wall increases from 0.086 milli-strain to 3.342 milli-strain.

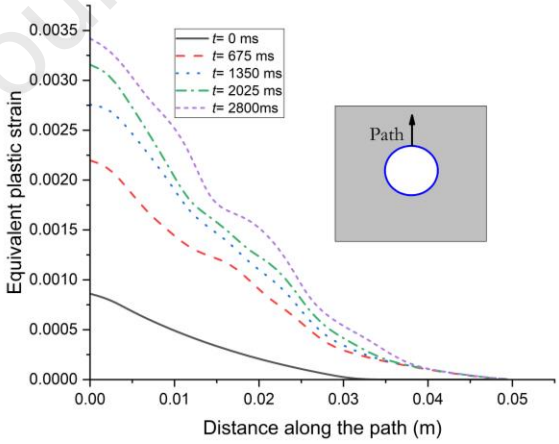

Fig. 15. Equivalent plastic strain before rock failure occurs (i.e. no elements are removed) as a function of normalized distance from the wellbore at t = 0 ms to t = 2800 ms.

The magnitude of the plastic strain and the radial dimension of the plastic zone vary along the wall, as there is randomness in where the drill-string hits. Fig. 16 represents the change in the equivalent plastic strain at two angles. Here, the horizontal axis is normalized by the length of each path, i.e., each curve is normalized by itself using the formula:

$$h = \frac{l}{l_p(t)} \quad (21)$$

where h is the value on the horizontal axis, l represents the actual distance along the path, and $l_p(t)$ is the radius of the zone that has yielded (i.e., where the equivalent plastic strain is not zero) at time t. The final point on each path corresponds to the location where the equivalent plastic strain reaches zero.

The vertical axis shows the equivalent plastic strain normalized with respect to its value at the wall using the following formula:

$$Y = \frac{\bar{\varepsilon}^{\mathrm{p}}(l)_t}{\bar{\varepsilon}^{\mathrm{p}}(l=0)_t} \quad (22)$$

where $\overline{\varepsilon^{\mathrm{p}}}(l)_t$ is the equivalent plastic strain at distance l along the path at time t, and $\overline{\varepsilon^{\mathrm{p}}}(l=0)_t$ is the equivalent plastic strain at the starting point of the path $l = 0$ at time t.

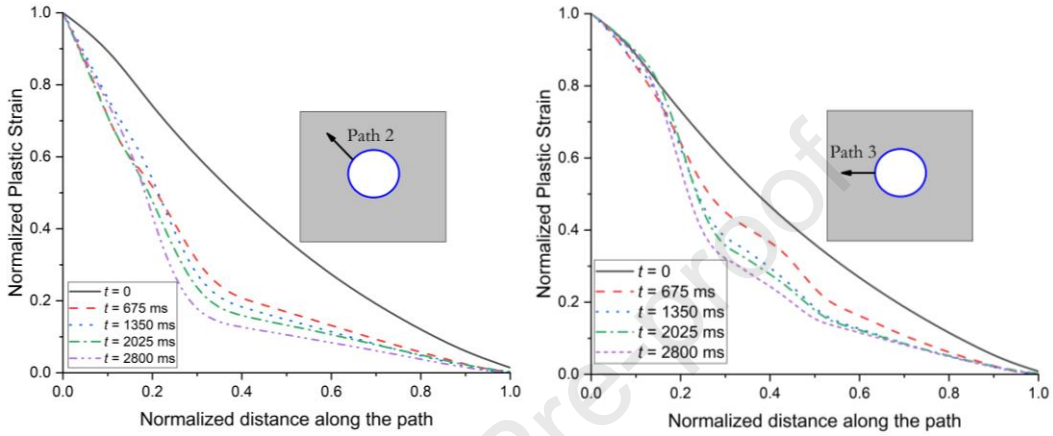

Fig. 16. Change in normalized equivalent plastic strain as a function of normalized distance at different time before failure along (a) path 2, and (b) path 3.

As may be seen in Fig. 16a and b; as time progresses (i.e. the number of impacts increases), there is a build-up of the equivalent plastic strain in the area close to the wellbore. Specifically, as the normalized distance increases, there is an initial sharp decline in normalized equivalent plastic strain. After reaching a certain point, the curve exhibits a more moderate decrease, resembling the behavior observed in the static balance case (i.e., at $t = 0$). This indicates the localization of damage and plastic strain near the wellbore, which consequently results in fatigue failure—a localized failure of the material.

6.2. Post failure dynamics

Once the rock-damage parameter in an element exceeds the predefined critical damage value, the element is removed from the analysis.

Determining the appropriate critical damage value for the failure and element removing criterion is essential because it is not easily measurable in experiments, yet it significantly influences the final results of the simulations (Ceretti et al., 1997).

According to the literature, the damage evolution of rocks under repeated loading can be categorized into three stages. Microcracks propagate and ultimately coalesce during the accelerated phase, culminating in macro failure (Wang et al., 2016). Accurately capturing this phase of damage in numerical simulations presents a significant challenge and requires considerable effort.

Based on experimental observations, as mentioned above, it is understood that the critical damage value should be reached within the third stage (since failure occur at this stage) and any critical damage value below the third stage may lead to unrealistic failure. Considering a damage value at the beginning of the third stage of the damage evolution is high enough for element deletion criterion.

However, adopting this value will result in the deletion of a large number of elements from the model during the deletion process. It is probable that some of these deleted elements might not fail under actual field conditions. Also, the deletion of too many elements will bring some drawbacks. One of the drawbacks is the loss of mass or energy due to element deletion (Gakwaya et al., 2009; Hu et al., 2018) which leads to violation of the energy conservation law.

By increasing the critical damage value, fewer elements will be deleted from the model in the early stages of the deletion process, making the model more stable in terms of mass conservation. However, a higher critical damage value leads to an increase in the stress concentration around the wellbore, which in turn increases the model instability. Consequently, it becomes challenging to accurately capture the final failure shape. While it is possible to observe rock failure in explicit Finite Element Method simulations after this point (i.e. after t=2960ms), the results are not reliable due to the violation of the energy conservation law.

Therefore, adjusting the critical damage value and comparing it with real-field condition is necessary to identify the accurate critical damage threshold.

In this study the critical damage value was set to 0.9. By considering this high value for critical damage, it can be confidently stated that the deleted elements would indeed fail in reality, although it results in the loss of capturing the final shape of the failed wellbore. However, by considering Fig. 9g to 9i the trend of failure is clear. The three small breakout zones at the top side of the wellbore visible in Fig. 9i will expand and eventually intersect at certain points, leading to a more extensive breakout failure. Fig. 17 represents the magnified version of Fig. 9i by focusing on the three small breakout zones.

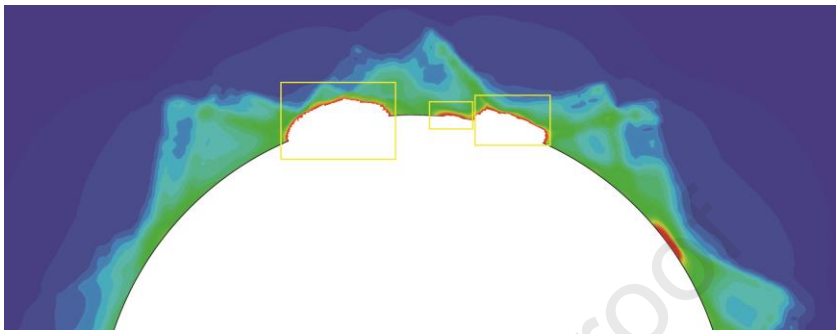

Fig. 17. The magnified version of Fig. 9i. The yellow boxes focus on small breakout zones.

As mentioned before, by considering a lower value of critical damage, more elements will be deleted from the simulation, but it is possible to see more details about the final shape of the failed wellbore. To illustrate this point, the final result obtained with the critical damage value equal to 0.75 is depicted in Fig. 18.

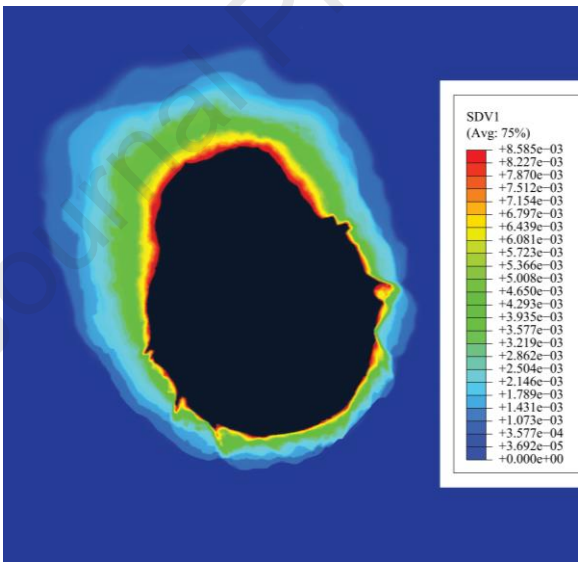

Fig. 18. The final shape of wellbore by considering the critical damage value equal to 0.75.

The final shape of the wellbore is in this case similar to breakout failure. Borehole breakouts occur when the borehole wall fails due to stress concentration (Shen et al., 2002). This failure leads to the elongation of the borehole's cross-section in the direction of the minimum principal stress (Shen et al., 2002; Haimson, 2007). However, it is important to note that the shape of failure in Fig. 18 is not a classically defined breakout failure, as the in-situ stress is hydrostatic in our simulations. Breakout failures typically occur in pairs, opposing each other across the wellbore (Dias et al., 2020), but as seen in Fig. 18, only one side of the wellbore cross-section has failed. This single-sided failure may serve as an indicator of drill string vibration-induced failure during wellbore inspection or logging.

Due to lack of information from the well under drill string repetitive loading considering the value of 0.9 is an optimistic choice. However, this optimistic approach also leads to failure of the wellbore.

It should be noted that increasing the critical damage value beyond the 0.9 makes the model highly unstable.

Fig. 19 illustrates the progression of rock fragmentation as the number of impacts increases when the critical damage value is equal to 0.9. As can be seen there is a sharp increase in the amount of fragmentation at the beginning of failure which can be considered as deceleration stage. By increasing the number of impacts, the rate of fragmentation will decrease, and the graph shows almost a steady and linear increase in fragmentation which can be considered as steady phase. At the end of this phase the model violates the energy conservation law, and it is not possible to see the complete trend of rock fragmentation accurately.

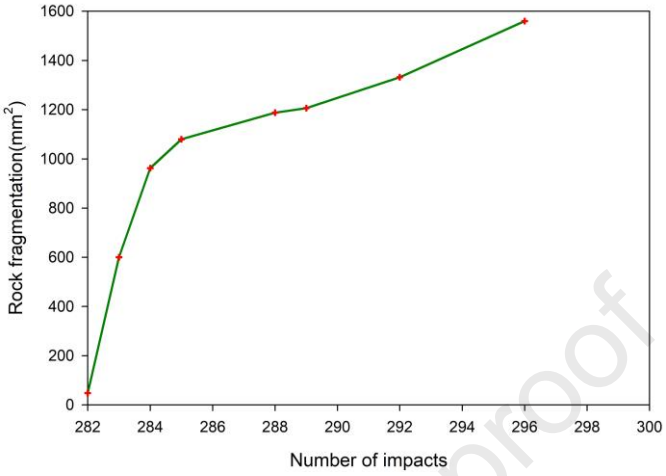

Fig. 19. The rock fragmentation over number of impacts with the critical damage value equal to 0.9.

By decreasing the critical damage value to 0.75, the fragmentation started at lower total number of impacts in comparison with the critical damage value equal to 0.9 as presented in Fig. 20. Once fragmentation started at the 271st cycle, the failed rock volume progressed in three distinct stages: initial deceleration, a steady phase, and finally, an acceleration stage that culminated in complete failure at the 288th stress cycle where energy conservation was violated. By comparing Fig. 19 and 20, it is clear that by increasing the critical damage value the simulation is not able to capture the third stage. It is crucial to acknowledge that the three-stage definition of rock fragmentation here should not be confused with the three stages of damage evolution. Indeed, all three stages of rock fragmentation are related to the final (third) stage of the damage evolution.

It is important to note that this interpretation requires further simulations and verification with real cases in the field for a better understanding.

The post-failure behavior as modeled here demands further investigation. What controls the shape of the borehole failure, and the volume of rock fragmentation are factors that impact the quality of drilling and subsequent wellbore stability.

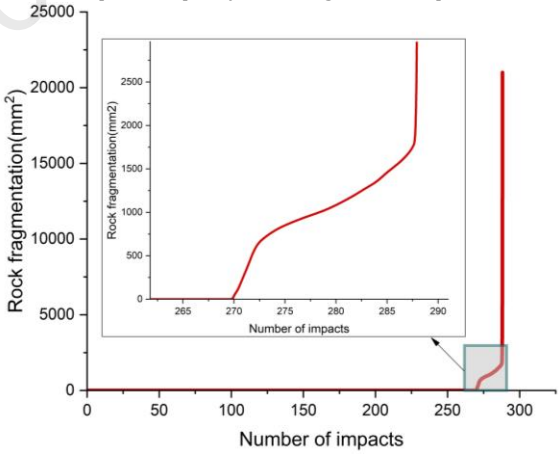

Fig. 20. The rock fragmentation over the number of impacts with more details on post-failure part when the critical damage value is equal to 0.75.

7. Conclusions

Repeated mechanical loading on the wellbore wall by the lateral drill string vibrations during drilling may lead to rock fatigue and subsequent wellbore instability. The purpose of this paper is to model the cyclic loading and wellbore failure by fatigue.

The absence of suitable constitutive models, capable of capturing the systematic material deterioration during repeated mechanical impacts, makes the numerical modeling of rock fatigue challenging. Also, the lack of objective information on both drill string dynamics and its implication to different rock types along the wellbore trajectory, makes wellbore stability due to cyclic loading a challenge. Having access to physically realistic numerical models that have been calibrated to realistic experiments may pave the way for further developments in predicting damage and will help to reduce drilling problems.

A new framework has been proposed in this study to mimic drill string-induced failure by fatigue. This framework is based on a robust elastoplastic constitutive model that is coupled with a damage model. In our numerical modeling run, a progressive damage acquired by the rock led to localized failure because of the randomly applied cyclic loading. Here, fatigue was modeled as a progressive failure mechanism that causes strength reduction of the rock. Both the magnitude of the plastic strain and the radius of the yielded zone increased during the repetitive impacts, compared to the static case. As such, repetitive impacts alter the mechanical response of the material.

During drilling operations, the repeated impacts by the drill string vibrations must be accounted for to avoid the progressing detrimental wellbore effects imposed by fatigue - also at impact stresses below static failure. We showed here how the plastic strain and yielded zone radius increased under repetitive impacts – and thus how failure develops rapidly once a certain threshold has been reached. Such processes require closer monitoring and potentially different engineering considerations than under static conditions.

Acknowledgments

This research was funded by the Norwegian Research Council, Equinor and Sekal with NFR (Grant No. 308826).

Declaration of competing interest

The authors declare that they have no known competing financial interests or personal relationships that could have appeared to influence the work reported in this paper.

References

Alizadeh, R., Marji, M. F., Abdollahipour, A., Sagand, M. P. 2023. Numerical simulation of fatigue crack propagation in heterogeneous geomaterials under varied loads using displacement discontinuity method. J. Rock Mech. Geotech. Eng. 15(3), 702-716.

Belytschko, T., Liu, W. K., Moran, B., Elkhodary, K. 2014. Nonlinear finite elements for continua and structures. John wiley & sons.

Cai, W., Dou, L., Ju, Y., Cao, W., Yuan, S., Si, G. 2018. A plastic strain-based damage model for heterogeneous coal using cohesion and dilation angle. Int. J. Rock Mech. Min. Sci. 110, 151-160.

Ceretti, E., Taupin, E., Altan, T. 1997. Simulation of metal flow and fracture applications in orthogonal cutting, blanking, and cold extrusion. CIRP Annals, 46(1), 187-190.

de Souza Neto, E. A., Peric, D., Owen, D. R. 2011. Computational methods for plasticity: theory and applications. John Wiley & Sons.

Dunayevsky, V., Abbassian, F., Judzis, A. 1993. Dynamic stability of drillstrings under fluctuating weight on bit. SPE drilling & completion, 8(2), 84-92.

Gakwaya, A., Zohra, F., Bahri, E. 2009. Impact damage and failure response of various aircraft structures under high velocity loading. Proceedings of the SIMULIA Customer Conference, London, England.

Haghgouei, H., Baghbanan, A., Hashemolhosseini, H., Jamali, S. 2021. Variable amplitude fatigue life prediction of rock samples under completely reversed loading. Geotech. Geol. Eng. 39, 1951-1962.

Haghgouei, H., Hashemolhosseini, H., Baghbanan, A., Jamali, S. 2018. The effect of loading frequency on fatigue life of green onyx under fully reversed loading. Exp. Tech. 42, 105-113.

Hu, X., Haris, A., Ridha, M., Tan, V., Tay, T. 2018. Progressive failure of bolted single-lap joints of woven fibre-reinforced composites. Compos. Struct., 189, 443-454.

Kamgue Lenwoue, A. R., Deng, J., Feng, Y., Li, H., Oloruntoba, A., Songwe Selabi, N. B., Marembo, M., Sun, Y. 2021. Numerical Investigation of the Influence of the Drill String Vibration Cyclic Loads on the Development of the Wellbore Natural Fracture. Energies 14(7), 2015.

Khaled, M. S. 2017. A new approach for predicting drillstring vibration impact on wellbore stability. SPE annual technical conference and exhibition.

Lenwoue, A. K., Deng, J., Feng, Y., Li, Z., Oloruntoba, A., Li, H., Selabi, N. S., Marembo, M. 2022. 3D numerical modeling of the effect of the drill string vibration cyclic loads on the wellbore natural fracture growth. J. Pet. Sci. Eng. 208, 109481.

Ma, T., Huang, J., Li, Z., Shi, Y., Jia, L., Zhong, C. 2022. Influence of drill-string lateral collision on wellbore stability of a horizontal well. Adv. Mech. Eng. 14(6), 16878132221107280.

Menčík, J. 2018. Impacts and vibrations. University of Pardubice.

Meng, M., Miska, S., Yu, M., Ozbayoglu, E. M. 2021. Mechanical behavior of Berea sandstone under cyclic loading: an application to dynamic loading of a wellbore. SPE J. 26(5), 2759-2779.

Meng, M., Miska, S. Z., Yu, M., Ozbayoglu, E. M. 2020. Fully coupled modeling of dynamic loading of the wellbore. SPE J. 25(3), 1462-1488.

Pašić, B., Gaurina Međimurec, N., Matanović, D. 2007. Wellbore instability: causes and consequences. Rudarsko-geološko-naftni zbornik, 19(1), 87-98.

Placido, J. o. C. R., Santos, H. l. M., Galeano, Y. D. 2002. Drillstring vibration and wellbore instability. J. Energy Res. Technol. 124(4), 217-222.

Santos, H., Placido, J., Wolter, C. 1999. Consequences and relevance of drillstring vibration on wellbore stability. SPE/IADC drilling conference.

Singh, A., Rao, K. S., Ayothiraman, R. 2019. An analytical solution to wellbore stability using Mogi-Coulomb failure criterion. J. Rock Mech. Geotech. Eng. 11(6), 1211-1230.

Wang, Y., Ma, L., Fan, P., Chen, Y. 2016. A fatigue damage model for rock salt considering the effects of loading frequency and amplitude. Int. J. Min. Sci. Technol. 26(5), 955-958.

Zhu, X., Liu, W. 2013. The effects of drill string impacts on wellbore stability. J. Pet. Sci. Eng. 109, 217-229.

Hadi Haghgouei is a PhD candidate in the Department of Geoscience and Petroleum at the Norwegian University of Science and Technology (NTNU), Norway. His research focuses on developing analytical and numerical models, with specific interests in mathematical modeling, creep, fatigue, fracture, and computational plasticity.

Declaration of interests

☒ The authors declare that they have no known competing financial interests or personal relationships that could have appeared to influence the work reported in this paper.

☐ The authors declare the following financial interests/personal relationships which may be considered as potential competing interests: